01 Jan 2010

Direct Numerical Simulation Of Hypersonic Turbulent Boundary Layers. Part 2. Effect Of Wall Temperature

L. (Lian) Duan
Missouri Unviersity of Science and Technology, duanl@mst.edu

I. Beekman

M. P. Martín

Recommended Citation

L. Duan et al., "Direct Numerical Simulation Of Hypersonic Turbulent Boundary Layers. Part 2. Effect Of Wall Temperature," *Journal of Fluid Mechanics*, vol. 655, pp. 419 - 445, Cambridge University Press, Jan 2010.
The definitive version is available at https://doi.org/10.1017/S0022112010000959

J. Fluid Mech. (2010), *vol.* 655, *pp.* 419–445. © Cambridge University Press 2010
doi:10.1017/S0022112010000959

Direct numerical simulation of hypersonic turbulent boundary layers. Part 2. Effect of wall temperature

L. DUAN, I. BEEKMAN AND M. P. MARTÍN†
Aerospace Engineering Department, University of Maryland, College Park, MD 20742, USA

(Received 28 May 2009; revised 18 February 2010; accepted 18 February 2010;
first published online 13 May 2010)

In this paper, we perform direct numerical simulation (DNS) of turbulent boundary layers at Mach 5 with the ratio of wall-to-edge temperature T_w/T_δ from 1.0 to 5.4 (Cases M5T1 to M5T5). The influence of wall cooling on Morkovin's scaling, Walz's equation, the standard and modified strong Reynolds analogies, turbulent kinetic energy budgets, compressibility effects and near-wall coherent structures is assessed. We find that many of the scaling relations used to express adiabatic compressible boundary-layer statistics in terms of incompressible boundary layers also hold for non-adiabatic cases. Compressibility effects are enhanced by wall cooling but remain insignificant, and the turbulence dissipation remains primarily solenoidal. Moreover, the variation of near-wall streaks, iso-surface of the swirl strength and hairpin packets with wall temperature demonstrates that cooling the wall increases the coherency of turbulent structures. We present the mechanism by which wall cooling enhances the coherence of turbulence structures, and we provide an explanation of why this mechanism does not represent an exception to the weakly compressible hypothesis.

1. Introduction

Boundary layers on both supersonic and hypersonic vehicles are compressible and mostly turbulent. One of the big differences between them is the wall-temperature condition. When a vehicle flies at supersonic speeds, the surface temperature is essentially adiabatic, while at hypersonic speeds, due to considerable radiative cooling and internal heat transfer, the external surface temperatures are significantly lower than the adiabatic wall temperature. As a result, the heat transfer between the boundary-layer flow and the surface of hypersonic vehicles is enormous. An accurate prediction of surface heat flux and the design of thermal protection system for hypersonic vehicles require a detailed understanding of non-adiabatic turbulent boundary layers.

An essential part of the study for compressible turbulent boundary layers is to check the validity of Morkovin's hypothesis. The hypothesis, first proposed by Morkovin (1962), is that, at moderate free-stream Mach numbers ($M \lessapprox 5$), dilatation is small and any differences from incompressible turbulence can be accounted for by mean variations of fluid properties. This is the basis for the van Driest transformation, a velocity scaling that accounts for the fluid-property variations to collapse compressible flow data onto the 'universal' incompressible distribution. To date, the validity of

---

† Email address for correspondence: pmartin@princeton.edu

Morkovin's hypothesis has been checked primarily using experimental investigations (see data compilation given by Fernholz & Finley 1980), and most of the experimental measurements are limited to basic turbulence quantities, such as mean and root mean square (r.m.s.) velocity and temperature and skin friction. There are only a limited number of numerical simulations which provide detailed turbulence statistics. For example, Guarini *et al.* (2000) and Pirozzoli, Grasso & Gatski (2004) performed direct numerical simulations (DNS) of supersonic turbulent boundary layers at Mach 2.5 and 2.25, respectively and found that the essential dynamics of the investigated supersonic turbulent boundary layers closely resemble the incompressible pattern under analogous conditions. Direct numerical simulations of compressible boundary layers at higher Mach numbers have also been performed by Martin (2004) and Maeder, Adams & Kleiser (2001) to check the possible breakdown of Morkovin's hypothesis, and Maeder (2000) investigated Morkovin's scaling under two surface conditions at Mach 4.5. Still, more work on the systematic investigation of compressibility effects and the validity of Morkovin's scaling under a wide range of non-adiabatic surface conditions is necessary.

Another important factor in compressible turbulent boundary-layer analysis is the strong Reynolds analogy (SRA), which relates the temperature fluctuations to the streamwise velocity fluctuations and is widely used to extend incompressible turbulence models to compressible flows. The SRA predicts that the velocity and temperature fluctuations are perfectly anticorrelated with the correlation coefficient $R_{u'T'} = -1$ (Morkovin 1962). As is shown by Lele (1994), this is only true for negligible pressure and total temperature fluctuations; the effects of non-negligible total temperature fluctuation on $R_{u'T'}$ and SRA can be extended given a known variation in mean total temperature (Gaviglio 1987). Guarini *et al.* (2000) presented a further derivation and analysis of the classic SRA equations and some extensions, and compared them with an adiabatic boundary-layer simulation at Mach number 2.5. The check of the validity of classic and modified SRA for supersonic boundary layers under adiabatic conditions has also been performed by Maeder *et al.* (2001) and Pirozzoli *et al.* (2004). As far as surface heat transfer is concerned, several modified forms of SRA have been proposed to take into account surface heat flux (Gaviglio 1987; Rubesin 1990; Huang, Coleman & Bradshaw 1995). Maeder (2000) checked the validity of the SRA for boundary layers at Mach 4.5 with two surface conditions and found that Huang's version of the modified SRA (Huang *et al.* 1995) demonstrated a considerable improvement of (4.1) of the SRA under cold wall conditions.

A major purpose of the current direct numerical simulations is to provide detailed statistics to evaluate theories such as Morkovin's hypothesis, the van Driest transformation, and the SRA under non-adiabatic conditions with a wide range of wall temperatures in more detail than has been previously possible.

Recent laboratory and numerical experiments indicate that, in addition to turbulence statistics, large-scale coherent structures play a key role in wall-bounded turbulent flows at incompressible and compressible conditions (Kim & Adrian 1999; Adrian, Meinhart & Tomkins 2000; Ganapathisubramani, Clemens & Dolling 2006; Hutchins & Marusic 2007; Ringuette, Wu & Martin 2008, amongst others). In the study of channel flow with isothermal walls, Coleman, Kim & Moser (1995) found that near-wall structures become more coherent with increasing Mach number and argued that the modified near-wall structures do not create an exception to the weekly compressible hypothesis. Morinishi, Tamano & Nakabayashi (2004) performed DNS of compressible turbulent channel flows between adiabatic and isothermal walls and showed that the near-wall velocity streaks are independent of the thermal wall

Case	M_δ	ρ_δ (kg m^{-3})	T_δ (K)	T_w/T_δ	T_w/T_r	Re_θ	Re_τ	$Re_{\delta 2}$	θ (mm)	H	δ (mm)
M5T1	4.97	0.0890	228.1	1.00	0.18	1279.1	798.1	1538.4	0.175	5.55	2.44
M5T2	4.97	0.0890	228.1	1.90	0.35	2300.2	624.7	1521.5	0.298	6.30	5.07
M5T3	4.97	0.0908	224.1	2.89	0.53	3011.6	522.2	1524.7	0.422	7.60	7.65
M5T4	4.97	0.0889	231.7	3.74	0.68	3819.3	433.8	1526.4	0.508	8.92	9.86
M5T5	4.97	0.0937	221.0	5.40	1.00	4840.5	385.9	1536.8	0.655	11.1	14.2

TABLE 1. Boundary-layer edge and wall parameters for the DNS database.

boundary conditions in semilocal units. Similar investigations of wall-temperature effects on turbulent structures have not yet been investigated in boundary layers. Therefore, another purpose of the current paper is to investigate the effects of heat transfer on large-scale coherent structures, as well as the possible influence of these large-scale structures on turbulence statistics in turbulent boundary layers using DNS data.

The paper is structured as follows. Flow conditions and simulation details are given in § 2. Turbulence statistics are given in § 3. SRA, turbulent kinetic energy (TKE) are given in §§ 4 and 5, respectively. Finally, the influence of wall temperature on compressibility effects is analysed in § 6 and the relationship between wall heat transfer and coherent structures is examined in § 7. Conclusions are presented in § 8.

2. Simulation details

2.1. *Flow conditions*

To study heat-transfer effects, we use a DNS database of turbulent boundary layers from Martin (2004, 2007) with nominal free stream Mach number 5 and wall-to-boundary-layer-edge temperature ratio T_w/T_δ ranging from 1.0 to 5.4. The boundary-layer edge conditions and wall parameters for the DNS database are given in table 1, which provides free stream Mach number, density and temperature (M_δ, ρ_δ and T_δ, respectively). The table also gives the following boundary-layer properties: momentum thickness θ, shape factor, $H=\delta^*/\theta$ (δ^* is the displacement thickness), boundary-layer thickness δ (defined as the location where the flow velocity is 99 % of that of the free stream) and Reynolds numbers, where $Re_\theta \equiv \rho_\delta u_\delta \theta/\mu_\delta$, $Re_\tau \equiv \rho_w u_\tau \delta/\mu_w$ and $Re_{\delta_2} \equiv \rho_\delta u_\delta \theta/\mu_w$. Re_{δ_2} was proposed by Fernholz & Finley (1980) and is defined by the ratio of the highest momentum ($=\rho_\delta u_\delta^2$) to the wall shear stress ($=\tau_w$).

For all cases, the wall condition is isothermal. The wall temperature for case M5T5 is prescribed to be nearly the adiabatic (recovery) temperature T_r, where $T_r \equiv T_\delta(1 + r((\gamma-1)/2)M_\delta{}^2)$ with recovery factor $r=0.9$. The prescribed wall temperatures decrease from M5T5 to M5T1.

The change in wall temperature inevitably changes the Reynolds number, since the flow density, viscosity, as well as the boundary-layer thickness vary as the wall temperature changes from one case to another. The simultaneous change in wall temperature and Reynolds number complicates the analysis. To study how turbulent boundary layers scale with wall temperature, it is desirable to match the Reynolds number for different wall-temperature cases in order to keep wall temperature as the only scaling parameter. Given the different definitions of Reynolds number and the large variation of fluid properties, a single Reynolds number is not sufficient to characterize the flow (Smits 1991; Lele 1994). Here, we report on the data analysis

Case	L_x/δ	L_y/δ	L_z/δ	Δx^+	Δy^+	z_2^+	α	N_x	N_y	N_z
M5T1	10.3	2.6	21.9	7.7	2.9	0.33	1.069	384	256	110
M5T2	7.9	2.0	15.8	7.8	3.0	0.32	1.069	384	256	110
M5T3	7.5	1.9	16.7	7.7	2.9	0.33	1.069	384	256	110
M5T4	7.8	1.9	16.4	7.5	2.8	0.33	1.069	384	256	110
M5T5	7.4	1.8	14.0	7.4	2.8	0.30	1.069	384	256	110

TABLE 2. Grid resolution and domain size for the direct numerical simulations.

following the approach of Fernholz & Finley (1980), matching $Re_{\delta 2}$ for the different wall-temperature cases. The same conclusions are drawn by matching Re_θ or Re_τ.

2.2. *Simulation method*

The governing equations, numerical methods and initialization procedure are given in Martin (2007). The working fluid is air. For computational efficiency, we use periodic boundary conditions in the streamwise and spanwise directions. Although the periodic boundary condition neglects streamwise inhomogeneity of the boundary layer and thus results in evolving mean flow and decaying turbulence, the usage is valid provided the turbulence is quasi-steady and sustains for sufficient time to gather statistics without apparent boundary-layer growth (see Xu & Martin 2004; Martin 2007). In particular, in the study of the inflow condition of compressible boundary layers, Xu & Martin (2004) showed that the data from the simulations with periodic boundary conditions are in good agreement with those obtained from the extended temporal simulations (Maeder *et al.* 2001), which shows the validity of the use of periodic boundary conditions.

For the current simulations, averages are computed over streamwise and spanwise directions of each field; then an ensemble average is calculated over fields spanning around one non-dimensional time unit. The time is non-dimensionalized by δ/u_τ, which corresponds to around $20\delta^*/u_e$. During this time period, the change in (δ, u_τ, C_f) is less than 5 % and thus the flow is a good approximation to a static station of a boundary layer (see Xu & Martin 2004).

2.3. *Simulation parameters*

Following Martin (2007), the computational domain size and grid resolution are determined based on the characteristic large length scale δ, and the characteristic small near-wall length scale z_τ, respectively. The computational domain must be large enough to contain a good sample of the large scales, while the grid resolution must be fine enough to resolve the near-wall structures. The domain size ($L_x \times L_y \times L_z$), the grid size ($\Delta x \times \Delta y \times \Delta z$) and the number of grid points ($N_x \times N_y \times N_z$) are given in table 2. We take the streamwise, spanwise and wall-normal directions to be x, y and z, respectively. Uniform grid spacings are used in the streamwise and spanwise directions with constant Δx^+ and Δy^+, where the superscript '+' indicates scaling with inner, or wall values. Geometric stretching is used in the wall-normal direction, with $z_k = z_2(\alpha^{k-1} - 1)/(\alpha - 1)$.

In the results that follow, both Reynolds and Favre averaging are used depending on simplicity of presentation and conventions previously used in the literature. The Reynolds average f over the x and y directions will be denoted by $\bar{f}$, or $\langle f \rangle$, and

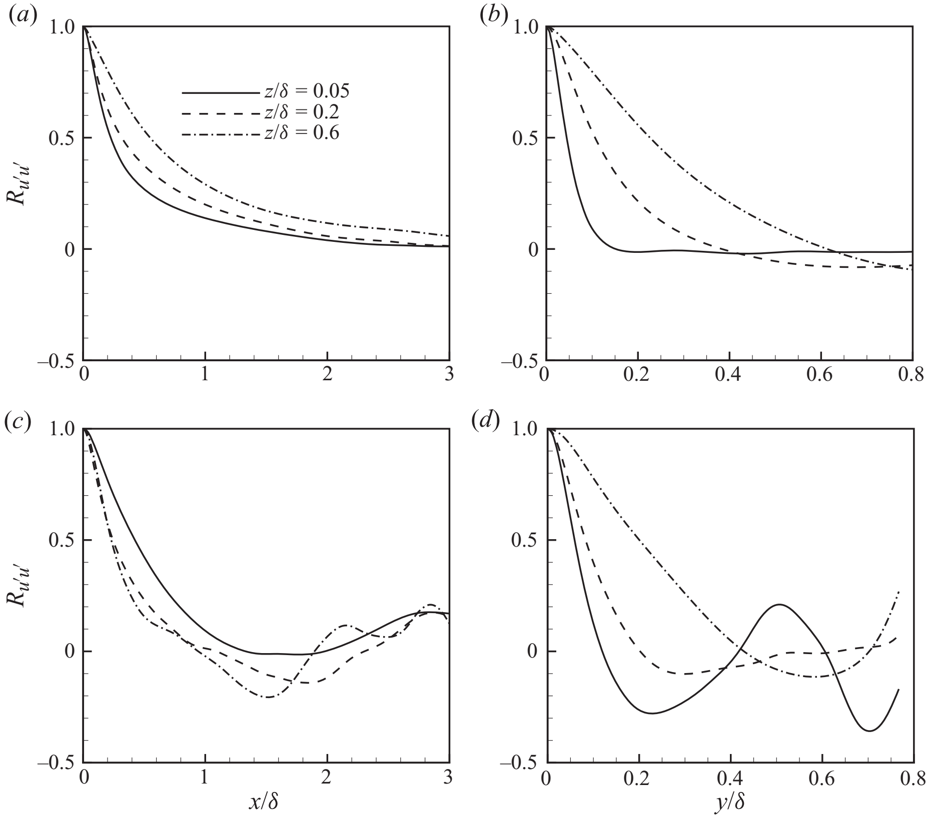

FIGURE 1. (*a*) Streamwise, and (*b*) spanwise two-point correlation for streamwise velocity component for M5T5; (*c*) streamwise, and (*d*) spanwise two-point correlation for streamwise velocity component for M5T1.

fluctuations about this mean will be denoted by f'. The Favre average over the x and y directions, $\tilde{f}$, is a density-weighted average:

$$\tilde{f} = \frac{\overline{\rho f}}{\overline{\rho}}.$$

Fluctuations about the Favre average will be denoted by f''.

To assess the adequacy of the domain size, streamwise and spanwise two-point correlations for the streamwise velocity component, $R_{u'u'}$, are plotted. Figure 1(*a*–*d*) shows that the streamwise and spanwise two-point correlations drop to zero for large separations. Similar results can be shown for all the other cases.

The grid resolution can be assessed by conducting grid convergence studies and examining the energy spectra. Figure 2(*a*–*d*) plots the density-weighted r.m.s. squared streamwise velocity normalized by the wall shear stress and r.m.s. temperature normalized by the mean temperature, respectively, for M5T5 and M5T1 with different number of grid points. All the curves collapse indistinguishably, indicating the grid is fine enough to converge the results. Grid convergence has been checked for all cases.

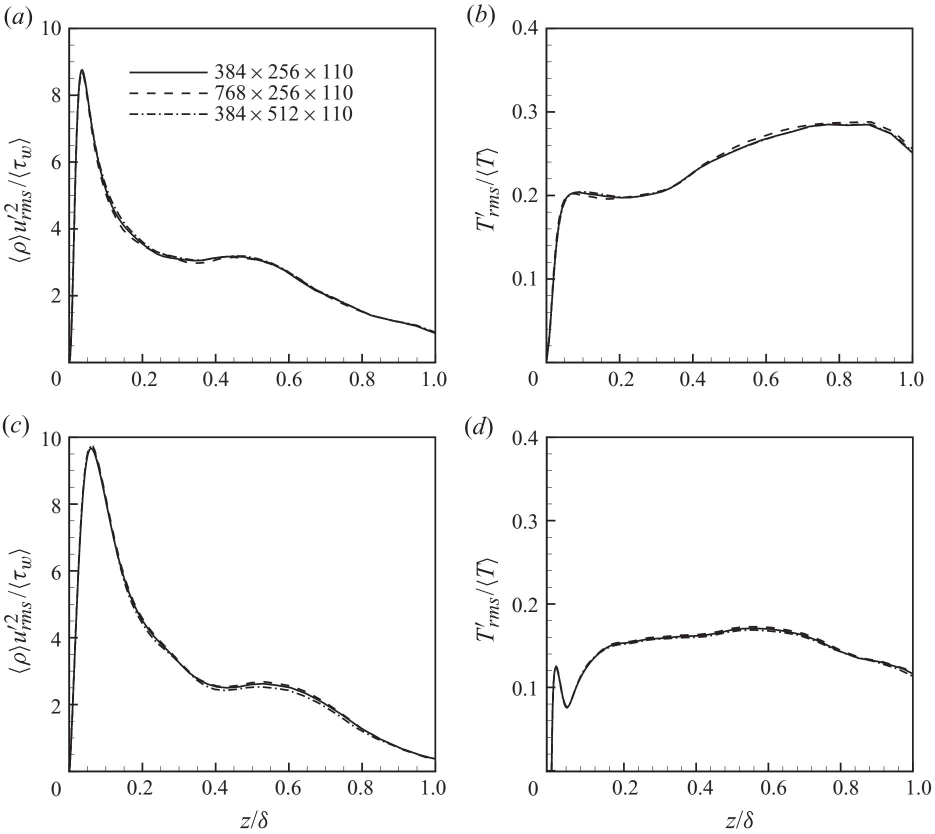

FIGURE 2. Grid convergence study for M5T5 (a, b) and M5T1 (c, d) varying grid size, $N_x \times N_y \times N_z$.

Figure 3 plots the energy spectrum at several wall normal locations for case M5T5. The energy distribution cascades down at least 8 orders of magnitude, indicating a good resolution of small scales. Similar results of energy spectrum can be obtained for other wall-temperature cases.

Another indication of the adequacy of the resolution is the value of $k_{max}\eta$, where k_{max} is the maximum wavenumber in x and η is the local Kolmogorov scale. The maximum and minimum of this value in the current DNS are 2.8 and 0.6, respectively, which is adequate. For comparison, the DNS of a supersonic boundary layer at Mach 2.5 conducted by Guarini *et al.* (2000) had values of 1.6 and 0.5 for the maximum and minimum of $k_{max}\eta$, respectively.

Further assessment of grid resolution near the wall can be conducted by comparing DNS calculated skin friction C_f and Reynolds analogy factor $2C_h/C_f$ with semi-empirical or experimental data. Here, C_h is the Stanton number defined as $\bar{q}_w/\bar{\rho}_\delta \bar{u}_\delta C_p(\bar{T}_w - \bar{T}_r)$, where $\bar{q}_w \equiv \bar{\kappa}(\partial \bar{T}/\partial z)|_w$.

Table 3 gives the DNS calculated skin friction, Stanton number and Reynolds analogy factor as well as the skin friction predicted by van Driest II theory (van Driest 1956). It is shown that DNS calculated skin frictions are within 5 % of the van Driest II prediction for all cases. In addition, the Reynolds analogy factors are about 1.1, which are within the predictions of experimental heat-transfer data (Hopkins & Inouye 1971).

Case	C_f	$(C_f)_{vandriest\,\Pi}$	C_h	$2C_h/C_f$
M5T1	2.46×10^{-3}	2.47×10^{-3}	1.39×10^{-3}	1.13
M5T2	2.05×10^{-3}	1.97×10^{-3}	1.14×10^{-3}	1.11
M5T3	1.81×10^{-3}	1.72×10^{-3}	9.77×10^{-4}	1.08
M5T4	1.50×10^{-3}	1.47×10^{-3}	8.39×10^{-4}	1.12
M5T5	1.28×10^{-3}	1.26×10^{-3}	NA	NA

TABLE 3. Skin friction and heat transfer of a hypersonic turbulent boundary layer with varying wall temperature.

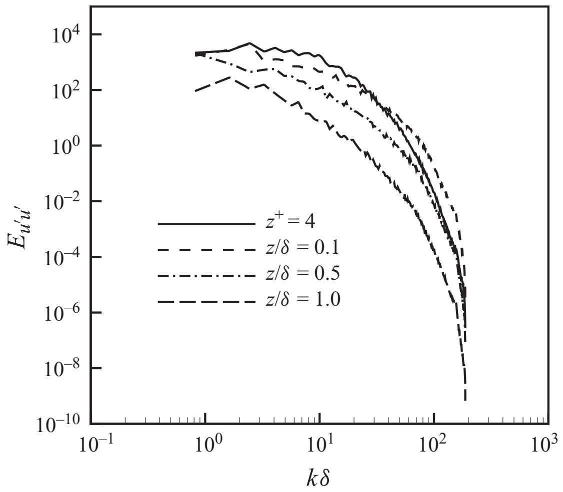

FIGURE 3. Two-dimensional energy spectra $E_{u'u'}$ at different wall normal locations for M5T5, where k is the wavenumber in the streamwise–spanwise plane.

3. Turbulence statistics

3.1. *Mean flow*

Figure 4(*a*, *b*) plots mean streamwise velocity and mean temperature, respectively, across the boundary layers for different wall-temperature cases. It is shown that the temperature gradient at the wall increases with decreasing wall temperature; at the same time, the maximum mean temperature location moves away from the wall. In addition, as the wall temperature decreases, the gradient of mean streamwise velocity near the wall decreases.

Figure 5 plots the van Driest transformed velocity, $\bar{u}^+_{VD}$, which is the density weighted mean velocity defined as

$$\bar{u}^+_{VD} = \int_0^{u^+} (\overline{\rho}/\overline{\rho}_w)^{1/2} \mathrm{d}u^+.$$

It is shown that the van Driest transformation collapses the profiles for different wall-temperature cases to the incompressible log law,

$$\overline{u}^+_{VD} = \frac{1}{\kappa} \ln z^+ + C$$

with k and C similar to the incompressible values, $\kappa \approx 0.41$ and $C \approx 5.2$ (Bradshaw 1977), and there is a clear logrithmic region at $30 \lessapprox z^+ \lessapprox 150$ for all the temperature

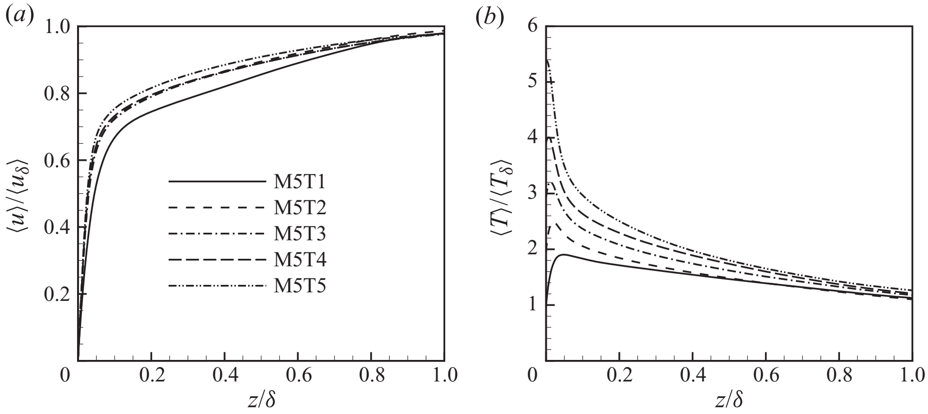

FIGURE 4. (*a*) Mean streamwise velocity, and (*b*) mean static temperature across the boundary layer for different wall-temperature cases.

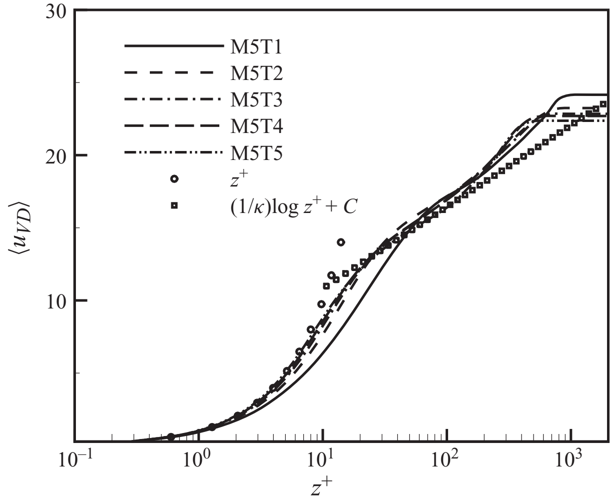

FIGURE 5. van Driest transformed velocity for different wall-temperature cases.

cases. In the simulation of compressible boundary layers with adiabatic and cold walls, Maeder (2000) found that the additive constant changes significantly with wall temperature, although the slope of $\overline{u}_{VD}^+$ is still given by $1/\kappa$; our results show that the additive constant is relatively insensitive to wall-temperature conditions.

In addition, it is shown in figure 5 that the region of linear viscous sublayer where $u_{VD}^+ = z^+$ shrinks significantly with decreasing wall temperature. For M5T1, $u_{VD}^+ = z^+$ is only satified until $z^+ \approx 2$ while for M5T5 it is satisfied until $z^+ \approx 8$. This is caused by the large gradient of mean fluid property at the wall for the cold wall case, where the rapid change in μ and ρ prevents the relation $\mu \partial \overline{u} / \partial z = \tau_w$ from being integrated to get $u_{VD}^+ = z^+$ except very close to the wall.

One of the commonly used temperature–velocity relationships for zero-pressure-gradient boundary layers is Walz's equation (Walz 1969):

$$\frac{\bar{T}}{\bar{T}_\delta} = \frac{\bar{T}_w}{\bar{T}_\delta} + \frac{\bar{T}_r - \bar{T}_w}{\bar{T}_\delta} \left(\frac{\bar{u}}{\bar{u}_\delta} \right) + \frac{\bar{T}_\delta - \bar{T}_r}{\bar{T}_\delta} \left(\frac{\bar{u}}{\bar{u}_\delta} \right)^2 . \tag{3.1}$$

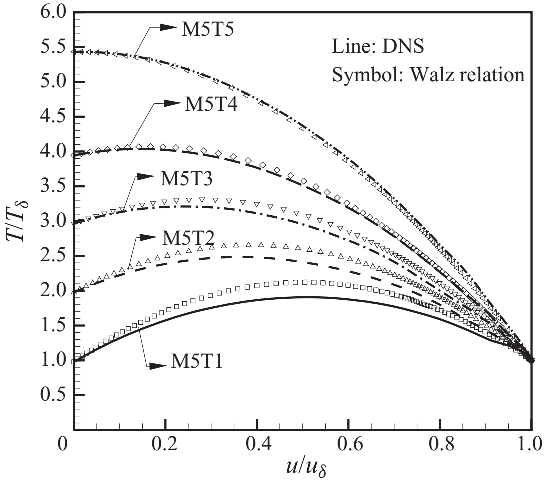

FIGURE 6. Test of Walz's equation, as expressed by (3.1) for different wall-temperature cases.

Voisinet & Lee (1972) evaluated the validity of (3.1) against experimental heat-transfer data at Mach 4.9 for $T_w/T_r = 1.0$, 0.8 and 0.25. They showed that the experimental data follow (3.1) fairly well except in the outer part of the boundary layer for all the wall conditions they considered.

Here we assess Walz's relation under a wider range of wall conditions. Figure 6 shows the comparison between (3.1) and the DNS results. For M5T5, the DNS results agree with (3.1). These results are consistent with the results by Pirozzoli *et al.* (2004), who performed DNS of a supersonic turbulent boundary layer at Mach 2.25 under adiabatic wall condition. As the wall temperature decreases, the mismatch between (3.1) and DNS results increases. For M5T1, the maximum mismatch is about 10 %.

3.2. *Turbulence quantities*

Figure 7(a, b) plots the normalized streamwise component of turbulence intensity with and without Morkovin's scaling, respectively. For comparison, the incompressible results by Spalart (1988) and the compressible adiabatic boundary layer results at Mach 4.5 by Maeder *et al.* (2001) have also been plotted. It is shown that when the density variation is taken into account, the profiles collapse much better for all temperature cases; the density scaling brings the magnitude of the compressible extrema closer to the incompressible ones of Spalart (1988), but the compressible peak values are higher than the incompressible ones, as also observed by Gatski & Erlebacher (2002) and Pirozzoli *et al.* (2004).

Figure 8(a–e) plots Reynolds stress $-\overline{\rho u'w'}$, mean viscous shear stress $\overline{\mu}(\partial\overline{u}/\partial\overline{z})$ and total shear stress for different wall-temperature cases. It is shown that there is a region of constant total shear stress, consistent with the wall condition $\partial\tau/\partial z = \partial p/\partial x (= 0)$. Similar results were reported by Guarini *et al.* (2000) and Pirozzoli *et al.* (2004) in the simulation of supersonic turbulent boundary layers at Mach 2.5 and 2.25, respectively.

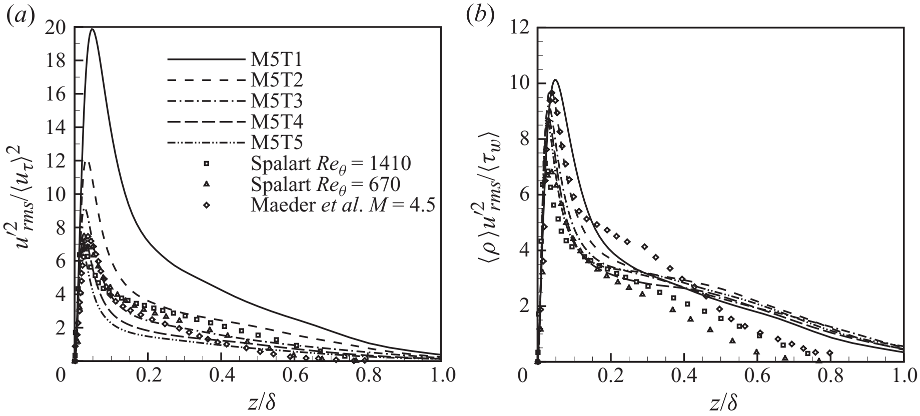

FIGURE 7. (*a*) $u'^2_{rms}/\bar{u}^2_\tau$ and (*b*) $\bar{\rho} u'^2_{rms}/\bar{\tau}_w$ across the boundary layer for different wall-temperature cases.

4. Reynolds analogies

4.1. *The strong Reynolds analogy*

Morkovin (1962) proposed five SRA relations. Three of them are as follows:

$$\frac{T''_{rms}/\tilde{T}}{(\gamma - 1){M_a}^2(u''_{rms}/\tilde{u})} \approx 1, \tag{4.1}$$

$$-R_{u''T''} \approx 1, \tag{4.2}$$

$$Pr_t = \frac{\overline{\rho u'' w''}(\partial \tilde{T}/\partial z)}{\overline{\rho w'' T''}(\partial \tilde{u}/\partial z)} \approx 1 \tag{4.3}$$

with $M_a^2 \equiv \tilde{u}^2/\gamma R \tilde{T}$.

Figure 9 plots the relationship between r.m.s. temperature and streamwise velocity fluctuations. We see that the left-hand side of (4.1) is a strong function of wall temperature, decreasing as wall temperature decreases. Equation (4.1) is only satisfied over $z/\delta < 0.6$ for case M5T5, consistent with the DNS of adiabatic turbulent boundary layers given by Guarini *et al.* (2000) and Martin (2007).

Several ‘modified’ forms of the SRA have been proposed to take the heat flux at the wall into account and remove wall-temperature dependence. For example, Cebeci & Smith (1974) derived an extended form of the strong Reynolds analogy (ESRA):

$$\frac{T''_{rms}/\tilde{T}}{(\gamma - 1){M_a}^2(u''_{rms}/\tilde{u})} \approx -\left[1 + C_p \frac{\tilde{T}_w - \tilde{T}_{t\delta}}{\tilde{T}} \frac{\tilde{u}}{\tilde{u}_\delta}\right]. \tag{4.4}$$

Gaviglio (1987), Rubesin (1990) and Huang *et al.* (1995) presented modified Reynolds analogies (GSRA, RSRA and HSRA, respectively) which have the form

$$\frac{T''_{rms}/\tilde{T}}{(\gamma - 1){M_a}^2(u''_{rms}/\tilde{u})} \approx \frac{1}{c(1 - (\partial \tilde{T}_t/\partial \tilde{T}))} \tag{4.5}$$

with $c = 1.0$, $c = 1.34$ and $c = Pr_t$, respectively.

To provide an assessment of the modified Reynolds analogies, figure 10(*a–e*) plots the ratio of the left-hand side of (4.4) and (4.5) to their right-hand side under different

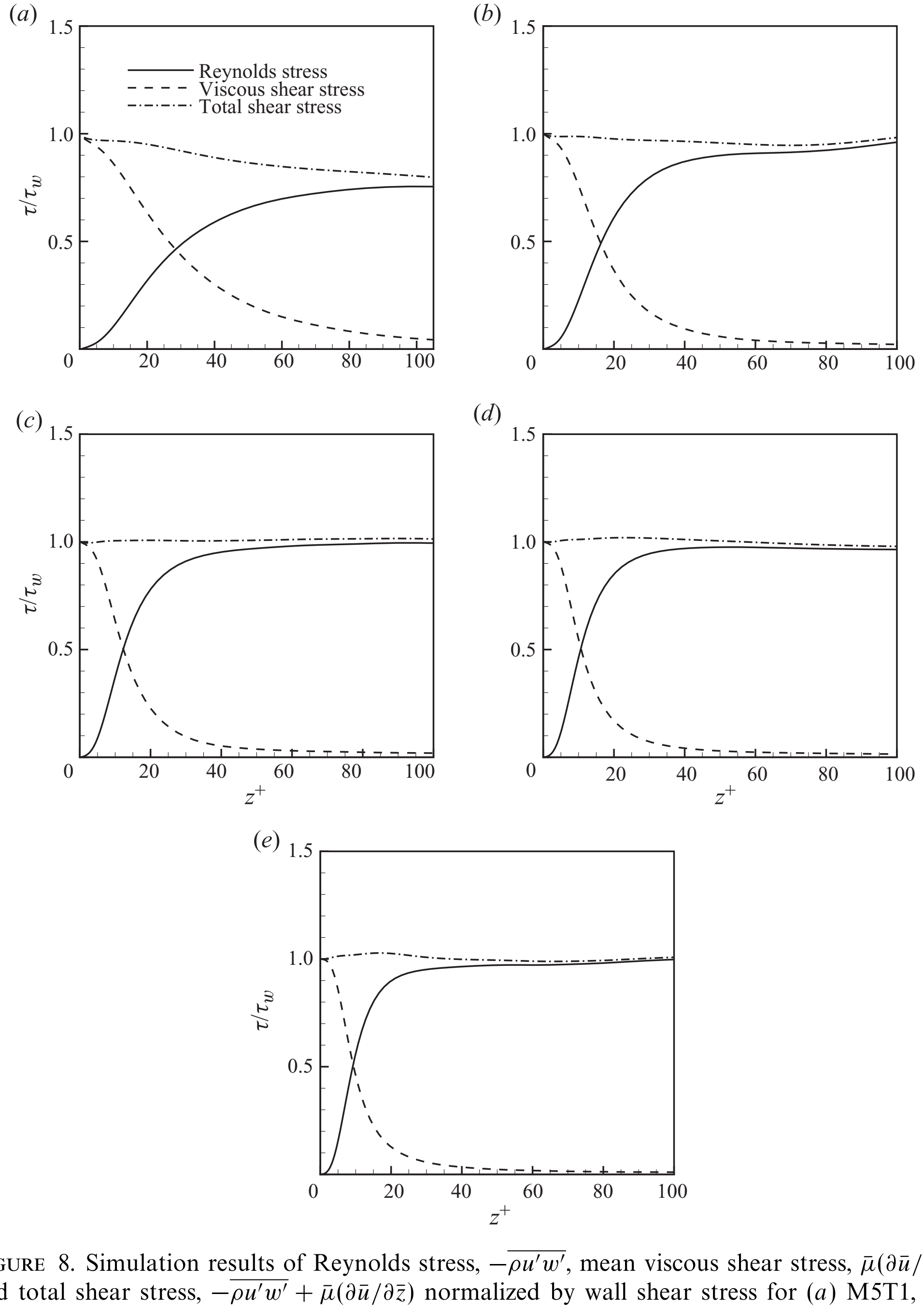

FIGURE 8. Simulation results of Reynolds stress, $-\overline{\rho u'w'}$, mean viscous shear stress, $\bar{\mu}(\partial\bar{u}/\partial\bar{z})$ and total shear stress, $-\overline{\rho u'w'} + \bar{\mu}(\partial\bar{u}/\partial\bar{z})$ normalized by wall shear stress for (*a*) M5T1, (*b*) M5T2, (*c*) M5T3, (*d*) M5T4 and (*e*) M5T5.

wall temperature conditions. The DNS data show that HSRA is the most accurate scaling which removes wall-temperature dependence of (4.1).

Figure 11 plots the correlation between temperature and velocity fluctuations across the boundary layer. We have chosen to take the correlation using centred Reynolds

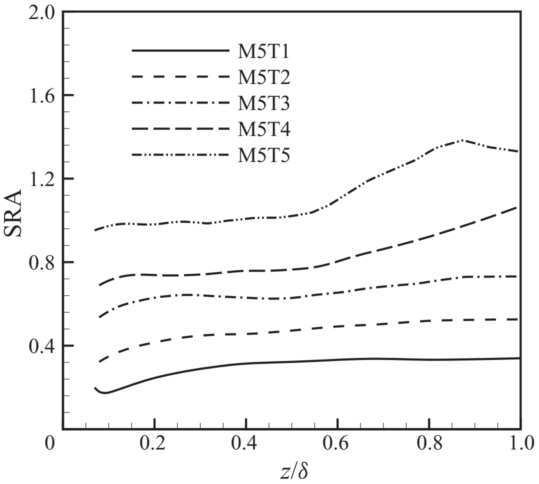

FIGURE 9. Test of the SRA, as expressed by (4.1) for different wall-temperature cases.

fluctuations, but the correlation using Favre fluctuations is nearly identical. It is shown that u' and T' are not perfectly anticorrelated for all wall-temperature cases. This is expected, since (4.1) was derived by assuming zero total temperature fluctuation, which is not true in the current simulation, as shown in figure 12. In addition, $-R_{u'T'}$ is nearly independent of wall temperature except close to the wall. Through most of the boundary layer, $-R_{u'T'}$ is approximately 0.6, similar to the results reported by Guarini *et al.* (2000), Maeder *et al.* (2001) and Martin (2007).

The major wall-temperature dependence of the correlation coefficient happens in a region close to the wall, where u' and T' have positive correlation when the wall is cooled. Also, we have noticed that for all cases, the crossover location, where $-R_{u'T'}=0$, nearly coincides with the location of maximum mean temperature.

This phenomenon can be explained as follows. The maximum temperature location moves away from the wall as the wall is cooled, and the sign of $-R_{u'T'}$ depends on that of the local mean temperature gradient. Ejection and sweep events will give a negative and positive value of u', respectively, but the sign of T' will be influenced by the sign of the mean temperature gradient. For ejections and sweeps, T' will be negative and positive, respectively, if the gradient of mean temperature is positive. As a result, $-R_{u'T'}$ will be negative if the gradient of mean temperature is positive, positive if the gradient of mean temperature is negative, and zero if the gradient of mean temperature is zero, which is the location of maximum mean temperature. This also partially explains why the crossover location of $-R_{u'T'}$ shifts farther away from the wall as the wall temperature decreases, because the maximum mean temperature location is also farther, as it is shown in figure 4(*b*). Similar phenomena of positive near-wall correlation have also been found in the DNS of strongly cooled channel flow (Coleman *et al.* 1995).

Figure 13 plots the turbulent Prandtl number across the boundary layer. Similar to $-R_{u'T'}$, Pr_t is insensitive to the wall temperature, and Pr_t is of order 1.

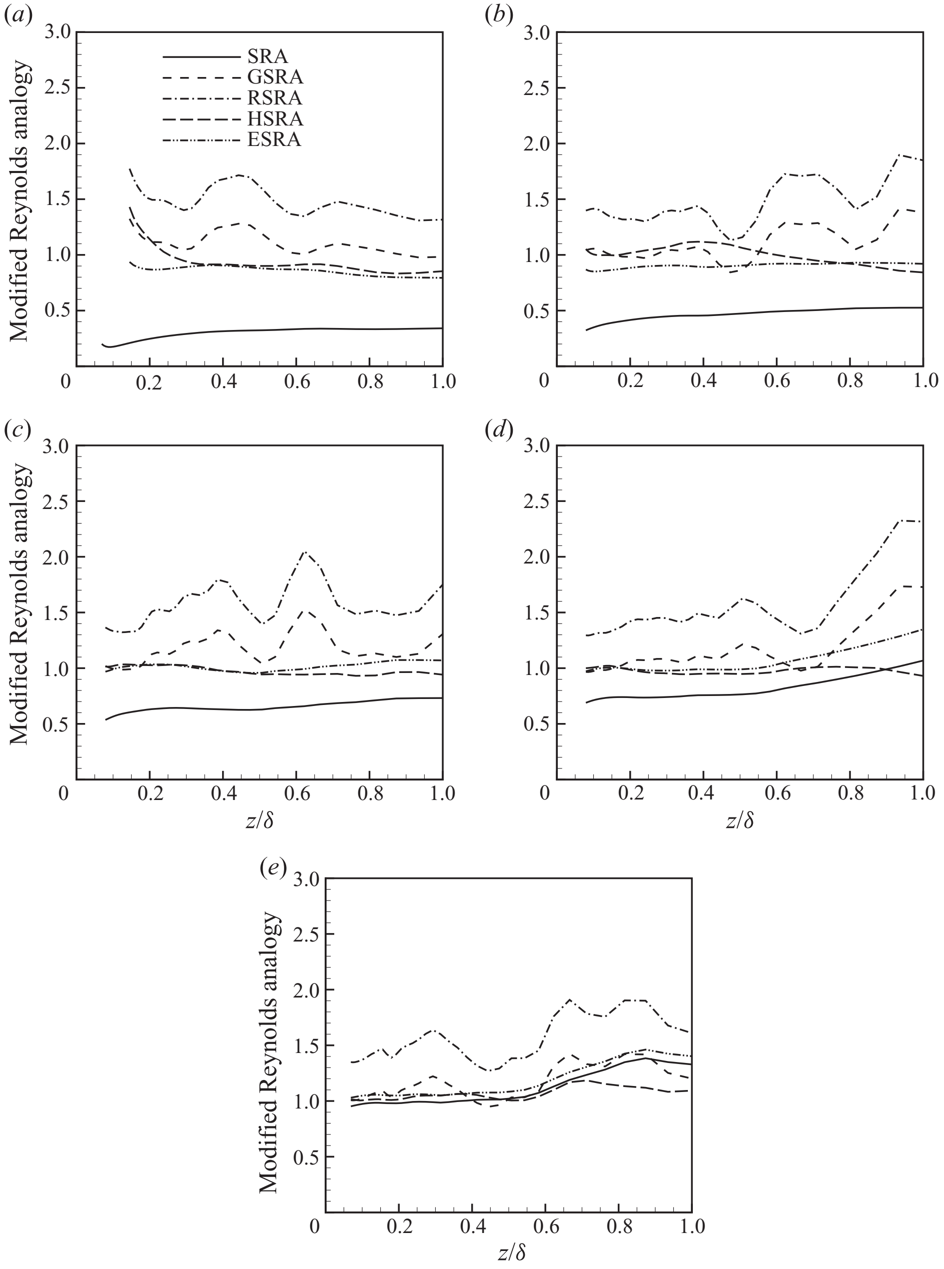

FIGURE 10. SRA, extended Reynolds analogy and modified Reynolds analogies of Gaviglio (1987), Rubesin (1990) and Huang *et al.* (1995) for (*a*) M5T1, (*b*) M5T2, (*c*) M5T3, (*d*) M5T4 and (*e*) M5T5.

5. Turbulent kinetic energy budget

The TKE is defined as

$$\tilde{k} = \frac{1}{2}\frac{\overline{\rho u_i'' u_i''}}{\overline{\rho}}$$

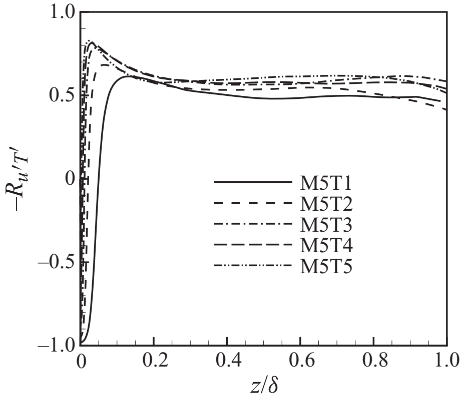

FIGURE 11. $-R_{u'T'}$ for different wall-temperature cases.

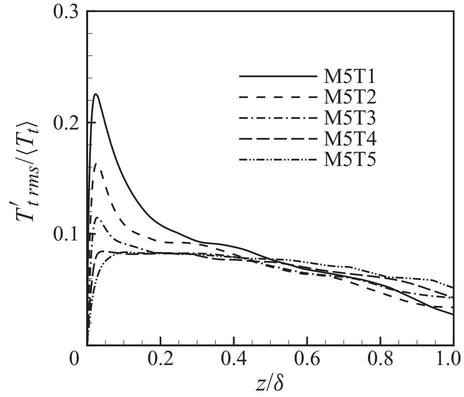

FIGURE 12. Root mean square of total temperature fluctuation normalized by local mean total temperature for different wall-temperature cases.

and the budget equation for TKE is given by

$$\frac{\partial}{\partial t}(\overline{\rho}\tilde{k}) + \tilde{w}\frac{\partial}{\partial z}(\overline{\rho}\tilde{k}) = P + T + \Pi + \phi_{dif} + \phi_{dis} + ST, \tag{5.1}$$

where

$$\begin{aligned}
P &= -\overline{\rho u_i'' w''}\frac{\partial \tilde{u}_i}{\partial z}, \\
T &= -\frac{1}{2}\frac{\partial}{\partial z}\overline{\rho u_i'' u_i'' w''}, \\
\Pi &= \Pi_t + \Pi_d = -\frac{\partial}{\partial z}\overline{w'' p'} + \overline{p'\frac{\partial u_i''}{\partial x_i}}, \\
\phi_{dif} &= \frac{\partial}{\partial z}\overline{u_i'' \tau_{iz}'}, \\
\phi_{dis} &= -\overline{\tau_{ij}'\frac{\partial u_i''}{\partial x_j}}, \\
ST &= -\overline{w''}\frac{\partial \overline{p}}{\partial z} + \overline{u_i''}\frac{\partial \overline{\tau_{ij}}}{\partial x_j} - \overline{\rho}\tilde{k}\frac{\partial \tilde{w}}{\partial z}.
\end{aligned}$$

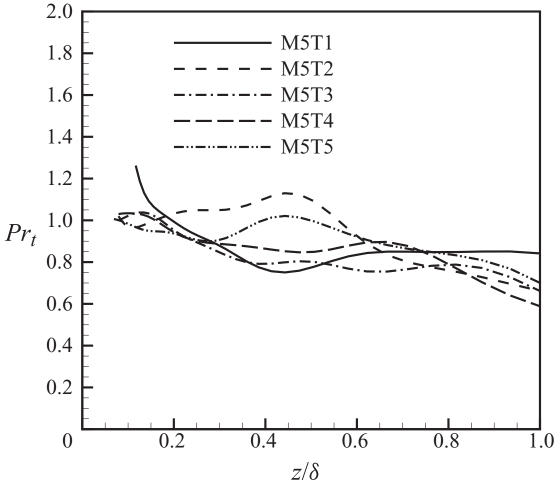

FIGURE 13. Pr_t for different wall-temperature cases.

The terms in (5.1) can be interpreted as follows: the left-hand side is the substantial derivative of the TKE along a mean streamline; P is the rate of production of TKE due to mean velocity gradient; T is turbulent transport; Π is the pressure terms (pressure diffusion and pressure dilatation, respectively); ϕ_{dif} is the viscous diffusion; ϕ_{dis} is the viscous dissipation; and ST represents terms that arise when the density is not constant. The first two terms of ST appear due to the difference between the Favre and Reynolds averaging and the third term is the production term due to dilatation. Besides terms in ST, pressure dilatation as well as dilatational dissipation are also due to non-constant density.

Figure 14(*a–f*) plots the terms in the budget of TKE normalized by conventional wall variables (defined in terms of the mean density, viscosity and shear stress at the wall). ST is small and has not been included on the plot. It is shown that the profiles for different wall-temperature cases do not collapse; the magnitude of TKE budget terms decreases with decreasing wall temperature, and the maximum values shift farther away from the wall.

In the study of compressible channel flows with isothermal walls, Coleman *et al.* (1995) demonstrated the importance of properly accounting for the mean property variations in the near-wall scaling and found that a much better collapse of data can be achieved if ‘semilocal’ scaling (Huang *et al.* 1995) is used instead (replacing $\overline{\rho}_w$ with $\overline{\rho}(z)$, u_τ with $u_\tau^* \equiv \sqrt{\tau_w/\overline{\rho}(z)}$, and $z_\tau^* \equiv \overline{\mu}(z)/(\overline{\rho}(z)u_\tau^*)$). The effectiveness of semilocal scaling has also been demonstrated by Maeder (2000) and Morinishi *et al.* (2004).

Figure 15(*a–f*) plots the TKE budget using semilocal scaling. It is shown that a much better collapse of the data is achieved. The minor difference in the peak value of the production term and the transport term might be due to Reynolds number effects. The success of semilocal scaling indicates that the major difference between budgets of an adiabatic wall and a cooled isothermal wall is mainly due to variations in mean fluid properties.

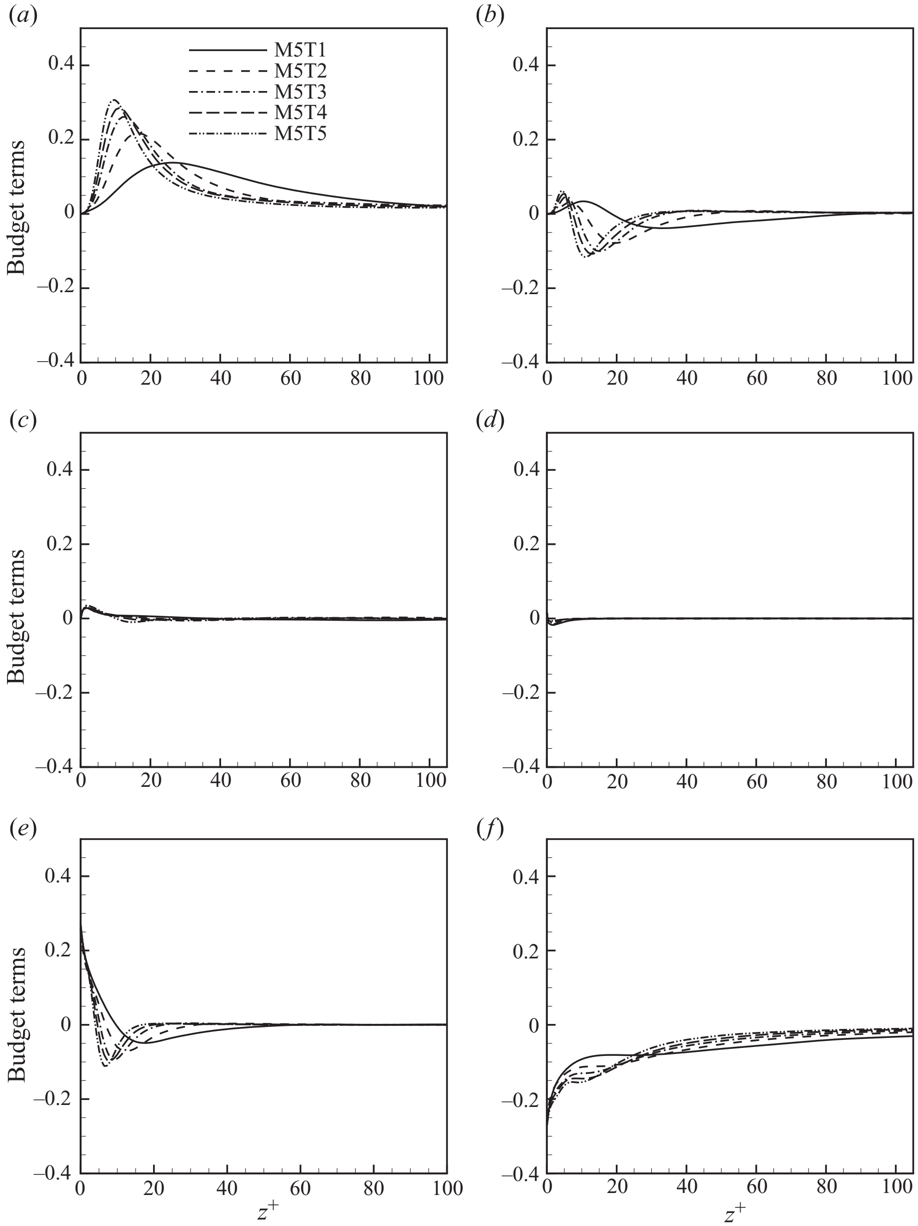

FIGURE 14. (*a*) Production, (*b*) turbulent transport, (*c*) pressure diffusion, (*d*) pressure dilatation, (*e*) viscous diffusion and (*f*) viscous dissipation plotted versus z^+. The variables are non-dimensionalized with $u_\tau \tau_w / z_\tau$.

6. Compressibility effects

6.1. *Turbulent Mach number*

An indicator for the significance of compressibility effects is the turbulent Mach number, defined by

$$M_t = \frac{(\overline{u_i' u_i'})^{1/2}}{\overline{a}}.$$

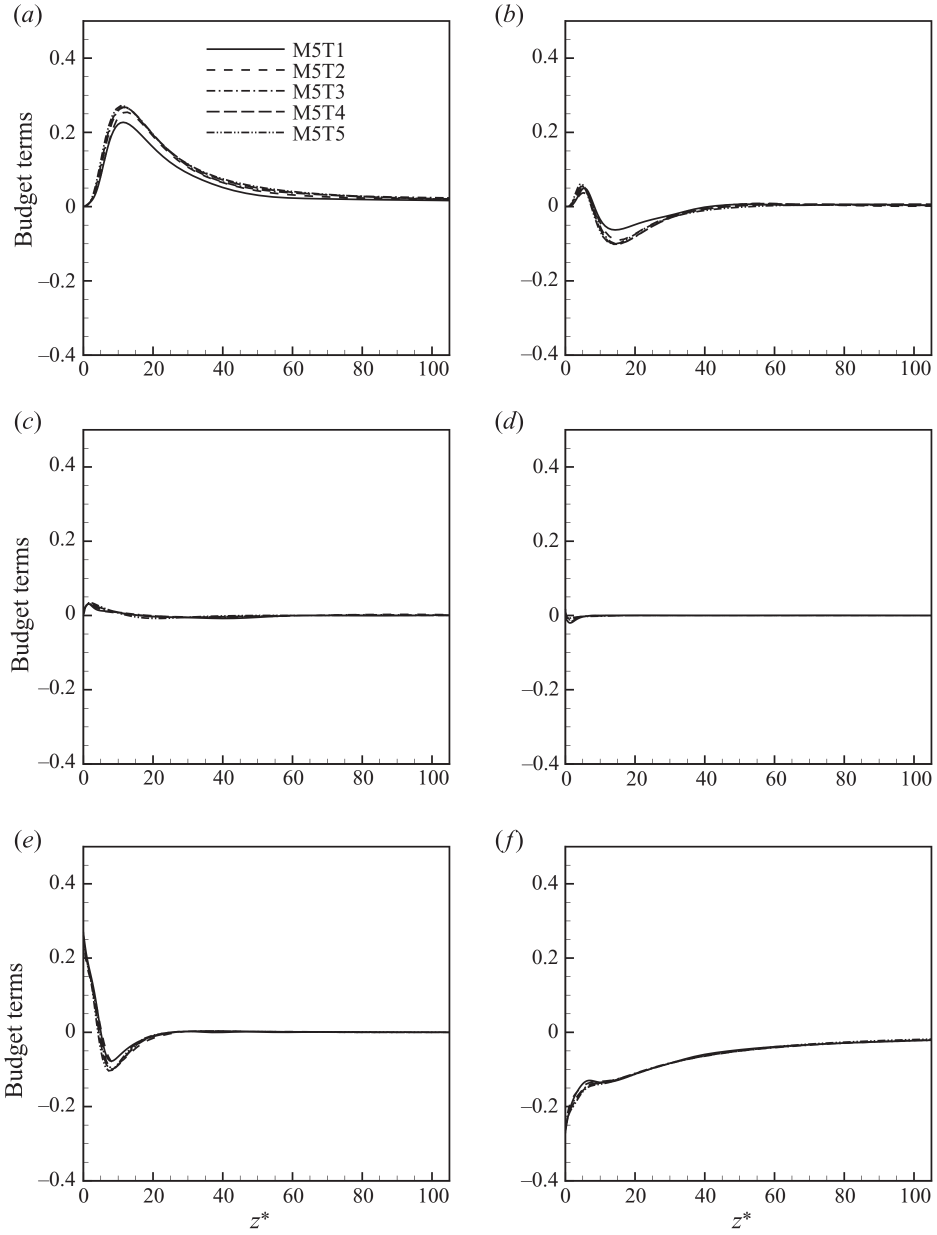

FIGURE 15. (*a*) Production, (*b*) turbulent transport, (*c*) pressure diffusion, (*d*) pressure dilatation, (*e*) viscous diffusion and (*f*) viscous dissipation in semilocal wall units. The variables are non-dimensionalized with $\overline{\rho} u_\tau^{*3}/z_\tau^*$ and $z^* = z/z_\tau^*$.

As wall cooling reduces $\overline{a}$, it is shown in figure 16(*a*) that the magnitude of M_t increases significantly with decreasing wall temperature. The peak value of M_t increases from about 0.35 for M5T5 to 0.5 for M5T1. The increase in M_t indicates stronger compressibility effects with wall cooling. A similar trend is observed for the fluctuating Mach number, M'_{rms}, which is the r.m.s. fluctuation of the Mach number and thereby includes temperature fluctuations, as shown in figure 16(*b*).

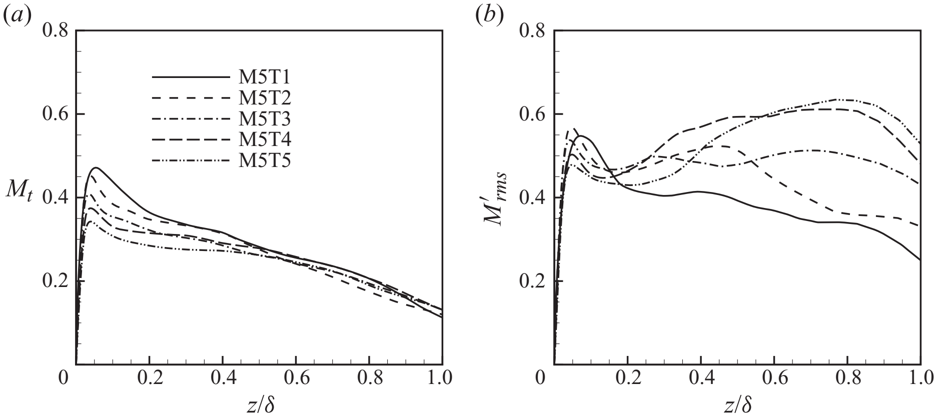

FIGURE 16. Simulation results of (*a*) turbulence Mach number, and (*b*) fluctuating Mach number for different wall-temperature cases.

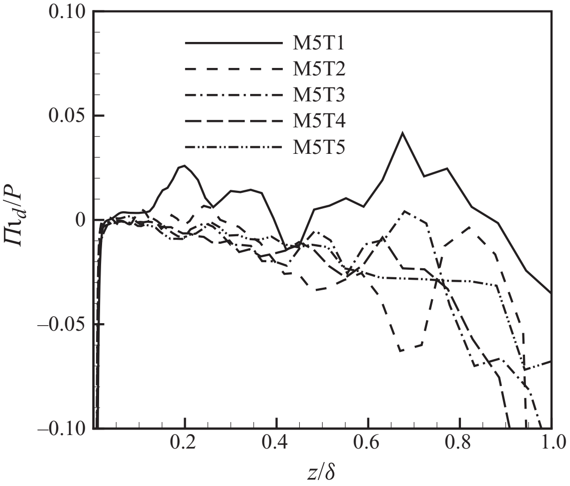

FIGURE 17. Π_d for different wall-temperature cases normalized by P.

It is commonly believed that 0.3 is the threshold of M_t above which compressibility effects become important for turbulence behaviour (Smits & Dussauge 2006). However, in the study of flat-plate boundary layers with Mach numbers 3, 4.5, 6, Maeder *et al.* (2001) showed that the intrinsic compressibility effects remain small for boundary layers with M_t significantly greater than the threshold. The success of Morkovin's scaling as well as the small values of dilation terms relative to production in the TKE budget support the argument by Maeder *et al.* (2001).

6.2. *Pressure dilatation and dilatational dissipation*

Compressibility effects can be further analysed by investigating terms that arise from the non-vanishing velocity divergence in TKE budgets. Figure 17 plots the pressure dilatation term $\Pi_d = \overline{p'(\partial u''_i/\partial x_i)}$ for different wall-temperature cases. To illustrate the relative importance of Π_d compared to relevant terms in the TKE budget, Π_d is normalized by the corresponding production term $P = -\overline{\rho u''_i w''}(\partial \tilde{u}_i/\partial z)$ in each case. It is shown that the pressure dilatation term is small relative to the production

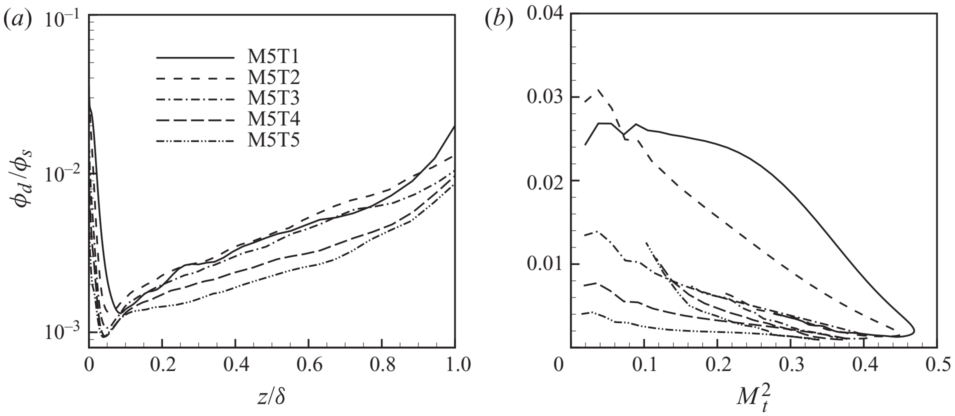

FIGURE 18. ϕ_d/ϕ_s versus (*a*) distance away from the wall, and (*b*) M_t^2 for different wall-temperature cases.

term, with maximum ratio less than 5 %. In addition, the relative importance of Π_d increases when the wall temperature decreases, indicating stronger compressibility effects with wall cooling. However, the compressibility effects remain insignificant.

Another term arising from the non-vanishing velocity divergence is the dilatational dissipation

$$\phi_d = \frac{4}{3}\overline{\mu}\overline{\frac{\partial u_i'}{\partial x_i}\frac{\partial u_k'}{\partial x_k}}. \tag{6.1}$$

The solenoidal dissipation is defined as

$$\phi_s = \overline{\mu}\overline{\omega_i'\omega_i'}, \tag{6.2}$$

where ω is the vorticity.

Figure 18(*a*) plots the ratio of ϕ_d to ϕ_s for different wall condition cases. It is shown that the ratio is very small, with maximum value less than 5 %; in most of the boundary layer, the ratio increases significantly with decreasing wall temperature, indicating stronger compressibility effects when the wall temperature is lowered.

Present approaches for modelling dilational dissipation can generally be cast into the form (Gatski 1997)

$$\phi_d/\phi_s = \alpha\mathscr{F}(M_t). \tag{6.3}$$

One of the simplest forms is $\mathscr{F} = M_t^2$ derived from homogeneous turbulence data by Gatski (1997). When the ratio ϕ_d/ϕ_s is plotted against M_t^2 (figure 18*b*), it is shown that this simple form fails, similar to the results reported by Huang *et al.* (1995), Maeder (2000) and Maeder *et al.* (2001).

7. Structure analysis

7.1. *Near-wall streaks*

In this section, we investigate the effects of wall temperature on near-wall streaks. Figure 19(*a*, *b*) plots the instantaneous streamwise velocity fluctuations at $z^+ = 15$ for M5T1 and M5T5, respectively. Several occurrences of very long regions of negative u fluctuation are identified as streaks and are visible in the plots as elongated dark regions. It is also shown that there is a decrease in spanwise meandering and increase in the streamwise coherency for M5T1 compared with M5T5, as also observed by

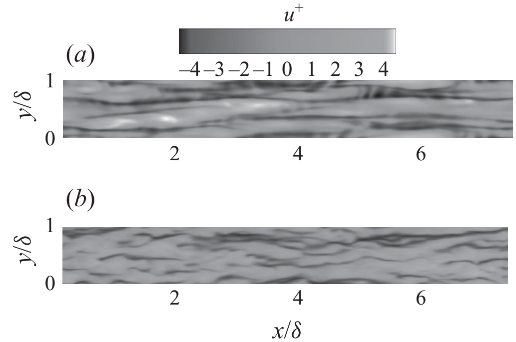

FIGURE 19. Instantaneous flow field at $z^+ = 15$ to visualize near-wall streaks for (*a*) M5T1 and (*b*) M5T5. Shading shows u fluctuations.

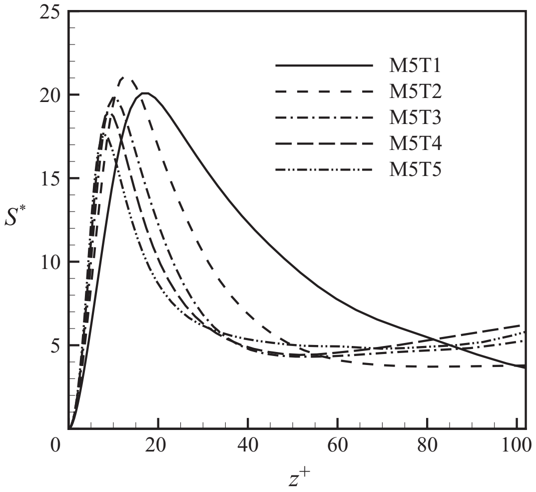

FIGURE 20. S^* for different wall-temperature cases.

Coleman *et al.* (1995) and Morinishi *et al.* (2004) in their simulations of compressible channel flows with isothermal walls.

Coleman *et al.* (1995) explained that the modification of near-wall streaks is caused by the change of turbulence-to-mean time scale ratio; however, Morinishi *et al.* (2004) found that there was no connection between the near-wall streak structures and the time-scale ratio. Our results confirmed the finding by Morinishi *et al.* (2004), as shown by figure 20, where the turbulence-to-mean time scale ratio S^*, where $S^* \equiv \overline{\rho} Sk/\phi_{dis}$ with $S = (\mathrm{d}\overline{u}/\mathrm{d}z)^{-1}$, is plotted for all temperature cases and there is no significant change in the time scale ratio.

One possible explanation for the increased streamwise coherency of near-wall streaks is the change in ‘anisotropy ratio’. Figure 21(*a*, *b*) plots the anisotropy ratios v'_{rms}/u'_{rms} and w'_{rms}/u'_{rms} for different wall-temperature cases. It is shown that the value of v'_{rms}/u'_{rms} decreases significantly as the wall is cooled. The anisotropy of fluctuations in the streamwise and wall-normal directions (w'_{rms}/u'_{rms}) also decreases with decreasing wall temperature; however, the relative differences between wall-temperature cases, especially very near the wall, are less significant. The increased deviation of anisotropy ratios from unity indicates reduced intensity of spanwise or

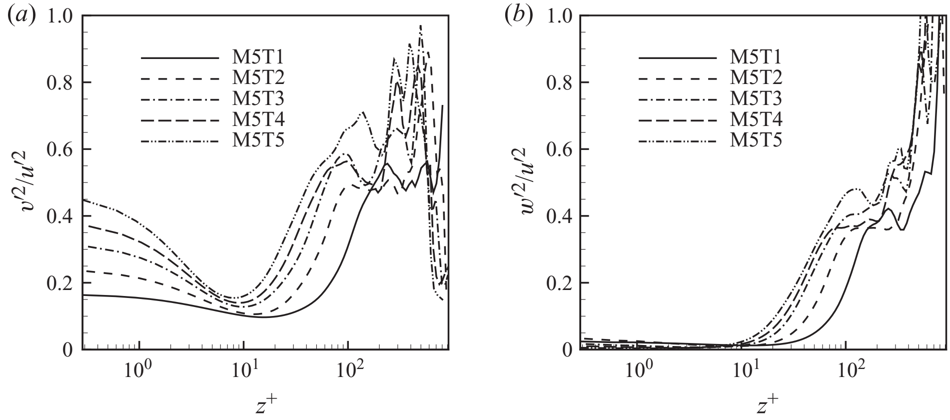

FIGURE 21. Anisotropy ratio (*a*) v'_{rms}/u'_{rms}, and (*b*) w'_{rms}/u'_{rms} for different wall-temperature cases.

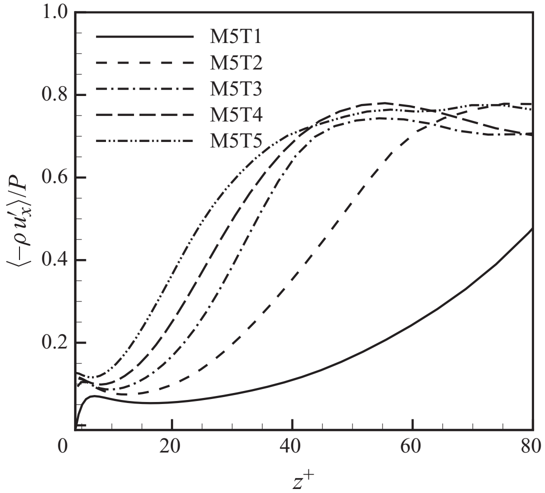

FIGURE 22. Ratio of streamwise pressure–strain term to production for all wall-temperature cases.

wall-normal fluctuations compared with those in the streamwise direction. As a result, less meandering and mixing happens in the spanwise and wall-normal directions and the streaks maintain their identity for longer streamwise extents.

The change in anisotropy ratio with wall cooling can also be understood from the energy point of view. Wall cooling is a sink of energy, which redistributes the energy between velocity components by influencing energy production and pressure–strain terms. We look at the kinetic energy budget for each velocity component of the turbulence. For boundary layers, energy is transferred from the mean flow to only the streamwise component of the fluctuating motion by $-\overline{\rho u'' w''}(\partial \tilde{u}/\partial z)$, and the pressure–strain rate term $\overline{p'(\partial u''/\partial x)}$ acts to exchange energy from streamwise to spanwise and wall-normal components of turbulent fluctuations. The relative importance of the energy exchange between components of the turbulence can be demonstrated by the ratio $R \equiv (\overline{p'(\partial u''/\partial x)})/(\overline{\rho u'' w''}(\partial \tilde{u}/\partial z))$, which gives a measure of the percentage of energy produced in the streamwise direction transferred to the other directions. Figure 22 plots the ratio R for cases M5T1 to M5T5. It is shown that

Case	$z^+=5$	$z^+=15$
M5T1	194.4	198.8
M5T2	126.5	136.9
M5T3	102.8	109.3
M5T4	87.8	96.0
M5T5	76.9	85.1

TABLE 4. Average spanwise streak spacing in wall units at $z^+=5$ and $z^+=15$ for different wall-temperature cases.

R decreases significantly as the wall temperature decreases, indicating significant reduction in energy exchange for the cold wall case. As a result, the kinetic energy gets accumulated in the streamwise direction and the streamwise turbulence motion becomes dominant over spanwise and wall-normal directions for the cold wall case.

As far as the spanwise spacing of near-wall streaks is concerned, it is widely believed that the average spanwise spacing is about 100 viscous wall units for subsonic turbulent boundary layers (Runstadler, Kline & Reynolds 1963; Bakewell & Lumley 1967; Kline *et al.* 1967). For supersonic boundary layers, Ringuette *et al.* (2006) showed that the average spanwise spacing is also about 100 viscous wall units, although it decreases when Mach number increases from 3 to 5. Morinishi *et al.* (2004) reported that the average spanwise spacing is about 100 semilocal wall units, as introduced in § 5, for compressible channel flows with isothermal walls. Table 4 gives the average spanwise spacing of near-wall streaks at both $z^+=5$ and 15 in viscous wall units for different wall-temperature cases. The velocity threshold used to determine spanwise streak spacing is $-0.1\,\overline{u}(z)$. It is shown that the average spanwise spacing increases significantly in viscous wall units with decreasing wall temperature for both locations. For the cold wall case, the average spacing is not ~100 wall units, as it is for the adiabatic case.

In the study of isothermal-wall channel flow, Coleman *et al.* (1995) argued that the modified turbulence structure with wall temperature does not represent an exception to the weakly compressible hypothesis. The validity of Morkovin's scaling in the current study supports this hypothesis.

7.2. *Hairpin vortices*

In this section, we investigate the influence of wall temperature on large-scale coherent structures or hairpin vortices and packets. The vortical structures of boundary layers are demonstrated by using both iso-surfaces of swirl strength (Zhou *et al.* 1999) and a correlation method after Brown & Thomas (1977).

Figure 23(a, b) plots iso-surfaces of the swirl strength for M5T1 and M5T5. It is shown that large-scale hairpin vortices are observed for different wall-temperature cases, and the vortical structures become fatter and less chaotic with decreasing T_w.

Next, hairpin vortices, packets and the corresponding low-momentum regions they encapsulate are inferred following Brown & Thomas (1977) by correlating the wall shear stress τ_w at a single reference location with streamwise mass flux (ρu) at locations surrounding the reference point. The correlation coefficient is defined by

$$R_{\tau_w(\rho u)} = \frac{\overline{\tau_w'(x, y)(\rho u)'(x+\Delta x, y+\Delta y, \Delta z)}}{\tau'_{w,rms}(\rho u)'_{rms}}. \tag{7.1}$$

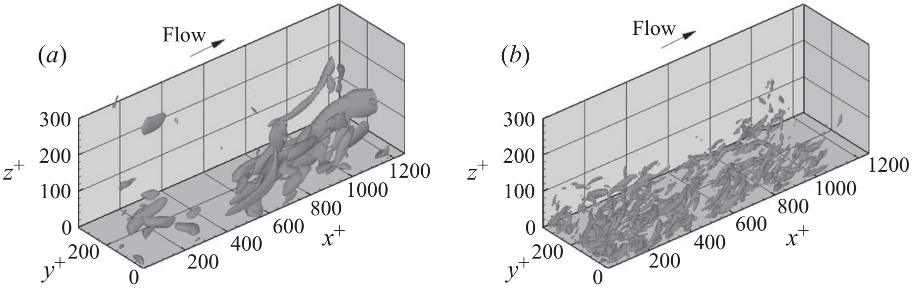

FIGURE 23. Iso-surface of λ_{ci} at $3.5\overline{\lambda_{ci}}$ to visualize vertical structure for (a) M5T1 and (b) M5T5.

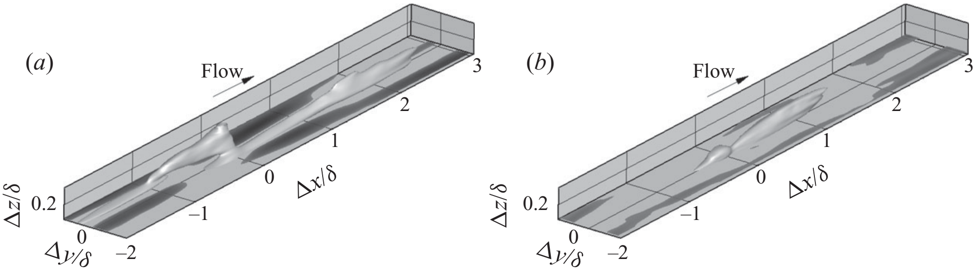

FIGURE 24. Iso-surface of $R_{\tau_w(\rho u)}$ to visualize vortical structure for (a) M5T1 and (b) M5T5. The iso-surface value of 0.13 (light) and the contour values immediately above the wall that are less than −0.02 (dark) are plotted.

Brown & Thomas (1977) inferred the existence of coherent structures based upon experimentally obtained profiles of $R_{\tau_w(\rho u)}$ versus Δx at several wall normal locations; here with the complete DNS flow fields, we compute the three-dimensional distribution of $R_{\tau_w(\rho u)}$ by simultaneously varying streamwise, spanwise and wall normal separations of (ρu) and τ_w, thus a more direct visualization of structures can be obtained.

Figure 24(a, b) plots the three-dimensional distribution of $R_{\tau_w(\rho u)}$ for M5T1 and M5T5, respectively. For both cases, the streamwise, spanwise and wall normal width of the viewing window are $-2\delta \leqslant \Delta x \leqslant 3\delta$, $-0.4\delta \leqslant \Delta y \leqslant 0.4\delta$ and $0.05 \leqslant \Delta z \leqslant 0.4\delta$, respectively, which are sufficient for the correlation to fall below 0.2. These plots show that for both cases, there is a positive region of $R_{\tau_w(\rho u)}$ in the middle surrounded by negative regions. This distribution of $R_{\tau_w(\rho u)}$ is directly related to the existence of hairpin vortices and packets. The positive region corresponds to low-momentum regions encapsulated by hairpin vortices or packets. Note the similarity in shape of this positive region with the region of induced low-speed fluid in the hairpin packet model of Adrian *et al.* (2000). Between the legs of a hairpin vortex, the ejection of fluid causes negative $(\rho u)'$ and negative τ_w', thus positive $R_{\tau_w(\rho u)}$. Outside the legs, the sweep events cause positive $(\rho u)'$, which correlates with the negative τ_w' between the legs to give negative $R_{\tau_w(\rho u)}$.

While both of these plots are strikingly similar to the conceptual model of Adrian *et al.* (2000), the stronger positive and negative values of the correlation coefficient for M5T1 compared with M5T5 indicate stronger more coherent hairpin packets when the wall is cooled. The increased signature of the older, upstream packet in the M5T1 case is evidence of greater alignment, organization and interaction between hairpin packets.

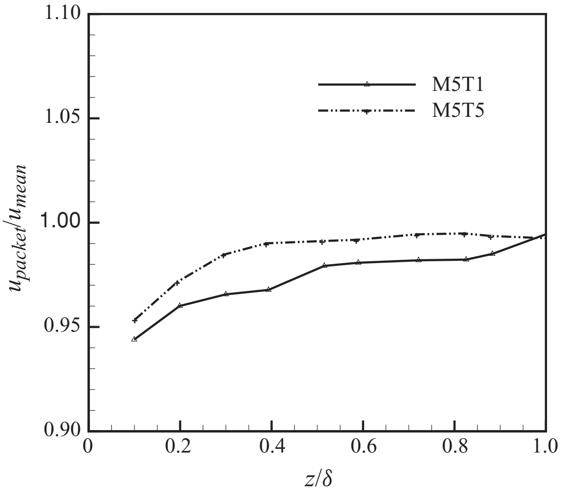

FIGURE 25. Ratio of average packet convection velocity to the mean flow velocity versus distance from the wall with the packet convection velocity computed after O'Farrell & Martin (2009).

The increased organization of hairpin packets with wall cooling can also be inferred by the average convection velocity of hairpin packets. Figure 25 plots the ratio of packet convection velocity to the mean flow velocity at different wall normal locations. The packet convection velocity is computed after Brown & Thomas by taking the conditional average of the streamwise velocity of points within each structure, as identified by $R_{\tau_w(\rho u)}$ exceeding a certain threshold (see O'Farrell & Martin 2009, for further details). The plot shows that there is a lag of packet convection velocity behind the mean, and the lag increases with decreasing wall temperature. The relatively slower convection velocity of hairpin packets most likely indicates that the hairpin vortices of the packets are more intense, more organized, or both, and therefore produce a relatively stronger backflow that retards the overall packet velocity. Consistently, the skin friction increases with decreased packet convection velocity.

8. Conclusion

We perform direct numerical simulations of Mach 5 turbulent boundary layers with wall-to-edge temperature ratio from 1.0 to 5.4 to study the effects of surface heat transfer on boundary-layer flow. It is shown that many of the scaling relations used to express adiabatic compressible boundary-layer statistics in terms of incompressible boundary layers also hold for non-adiabatic cases. In particular, we have shown that the van Driest transformed velocity collapses different wall-temperature results with the incompressible results. It is also shown that the r.m.s. velocity fluctuations of the varying wall-temperature results better collapse with the adiabatic results by using the mean density scaling suggested by Morkovin.

It is found that the mean static temperature field exhibits a quadratic dependence upon the mean velocity, as predicted by Walz's equation (3.1), for the adiabatic case. However, the deviation from the predicted quadratic dependence increases with decreased wall temperature, and the largest mismatch is up to 10 % for $T_w/T_\delta = 1.0$ in the present study.

We find that u' and T' are not perfectly anticorrelated (as predicted by the SRA, see (4.2)), and, in the presence of wall cooling, $R_{u'T'}$ remains about the same between the different wall-temperature cases, except near the wall. The left-hand side of (4.1) strongly depends on wall temperature, and the assessment of extended forms shows Huang's version is a good scaling for wall temperature. Also, the turbulent Prandtl number is nearly constant for most of the boundary layer and insensitive to wall-temperature condition.

The TKE budget was calculated and compared for all wall-temperature cases. It is shown that conventional inner scaling does not collapse the data. However, the semilocal scaling that takes into account local variation of fluid properties better collapses the data.

The profiles of M_t, M'_{rms} show that compressibility effects increase with decreasing wall temperature. However, terms arising from the non-vanishing velocity divergence in TKE budgets, such as pressure dilatation and dilatational dissipation, remain small and the wall temperature influences the TKE largely by affecting the terms that appear in the incompressible case. In addition, our boundary-layer data show that the modelling approach for dilatational terms, which was developed based on homogeneous turbulence data, fails to predict compressibility effects in boundary layers correctly, consistent with the study by Maeder *et al.* (2001).

Wall cooling has the effect of reducing the apparent chaos of the turbulent structures. We have seen that the near-wall streaks become more coherent with decreasing wall temperature, similar to the obervations of Coleman *et al.* (1995) and Morinishi *et al.* (2004). In addition, with wall cooling vortical structures become larger and less chaotic, as shown in figure 23. The strength of and organization between hairpin packets, appears to increase with decreasing wall temperature. This is observed in the iso-surface of $R_{\tau_w(\rho u)}$, the average packet convection velocity, and the skin friction coefficient.

We show that this modified turbulence structure is a result of the decreased relative importance of the inter-component transfer of TKE with wall cooling, rather than the transfer of energy between the kinetic and internal modes due to direct compressibility effects. As the wall is cooled, the relative energy transfer to the wall-normal and spanwise velocity components is decreased. As a result, the anisotropy ratio near the wall deviates further from unity with wall cooling, and eddies travelling in the spanwise or wall normal directions have less kinetic energy to disrupt the coherent structures. This explanation further supports Coleman's argument that the modified turbulence structure with wall temperature does not represent an exception to the weakly compressible hypothesis.

This work is supported by NASA under Cooperative Agreement NNX08ADO4A directed by Peter Gnoffo. A portion of this work was done in Princeton University.

REFERENCES

Adrian, R., Meinhart, C. & Tomkins, C. 2000 Vortex organization in the outer region of the turbulent boundary layer. *J. Fluid Mech.* **422**, 1–54.

Bakewell, H. P. & Lumley, J. L. 1967 Viscous sublayer and adjacent wall region in turbulent pipe flow. *Phys. Fluids* **10** (9), 1880–1889.

Bradshaw, P. 1977 Compressible turbulent shear layers. *Annu. Rev. Fluid Mech.* **9**, 33–54.

Brown, G. L. & Thomas, A. S. W. 1977 Large structure in a turbulent boundary layer. *Phys. Fluids* **20** (10), S243–S252.

Cebeci, T. & Smith, A. M. O. 1974 *Analysis of Turbulent Boundary Layers*. Academic.

Coleman, G. N., Kim, J. & Moser, R. D. 1995 A numerical study of turbulent supersonic isothermal-wall channel flow. *J. Fluid Mech.* **305**, 159–183.

van Driest, E. R. 1956 The problem of aerodynamic heating. *Aeronaut. Engng Rev.* **15** (10), 26–41.

Fernholz, H. H. & Finley, P. J. 1980 A critical commentary on mean flow data for two-dimensional compressible boundary layers. AGARD-AG-253.

Ganapathisubramani, B., Clemens, N. & Dolling, D. 2006 Large-scale motions in a supersonic turbulent boundary layers. *J. Fluid Mech.* **556**, 1–11.

Gatski, T. B. 1997 *New Tools in Turbulence Modelling*. Springer.

Gatski, T. B. & Erlebacher, G. 2002 Numerical simulation of a spatially evolving supersonic turbulent boundary layer. *Tech. Rep.* TM-211934. NASA.

Gaviglio, J. 1987 Reynolds analogies and experimental study of heat transfer in the supersonic boundary layer. *Intl J. Heat Mass Transfer* **30** (5), 911–926.

Guarini, S. E., Moser, R. D., Shariff, K. & Wray, A. 2000 Direct numerical simulation of a supersonic turbulent boundary layer at mach 2.5. *J. Fluid Mech.* **414**, 1–33.

Hopkins, E. J. & Inouye, M. 1971 Evaluation of theories for predicting turbulent skin friction and heat transfer on flat plates at supersonic and hypersonic mach numbers. *AIAA J.* **9** (6), 993–1003.

Huang, P. G., Coleman, G. N. & Bradshaw, P. 1995 Compressible turbulent channel flows: DNS results and modelling. *J. Fluid Mech.* **305**, 185–218.

Hutchins, N. & Marusic, I. 2007 Evidence of very long meandering features in the logarithmic region of turbulent boundary layers. *J. Fluid Mech.* **579**, 1–28.

Kim, K. C. & Adrian, R. J. 1999 Very large-scale motion in the outer layer. *Phys. Fluids* **11** (2), 417–422.

Kline, S. J., Reynolds, W. C., Schraub, F. A. & Runstaller, W. P. 1967 *J. Fluid Mech.* **30**, 741–773.

Lele, S. K. 1994 Compressibility effects on turbulence. *Annu. Rev. Fluid Mech.* **26**, 211–254.

Maeder, T. 2000 Numerical investigation of supersonic turbulent boundary layers. PhD thesis, ETH, Zürich.

Maeder, T., Adams, N. A. & Kleiser, L. 2001 Direct simulation of turbulent supersonic boundary layers by an extended temporal approach. *J. Fluid Mech.* **429**, 187–216.

Martin, M. P. 2004 DNS of hyersonic turbulent boundary layers. *AIAA Paper 2004-2337*.

Martin, M. P. 2007 Direct numerical simulation of hypersonic turbulent boundary layers. Part 1. Initialization and comparison with experiments. *J. Fluid Mech.* **570**, 347–364.

Morinishi, Y., Tamano, S. & Nakabayashi, K. 2004 Direct numerical simulation of compressible turbulent channel flow between adiabatic and isothermal walls. *J. Fluid Mech.* **502**, 273–308.

Morkovin, M. V. 1962 Effects of compressibility on turbulent flows. In *Mécanique de la Turbulence* (ed. A. Favre), pp. 367–380. CNRS.

O'Farrell, C. & Martin, M. P. 2009 Chasing eddies and their wall signature in DNS data of turbulent boundary layers. *J. Turbul.* **10** (15), 1–22.

Pirozzoli, S., Grasso, F. & Gatski, T. B. 2004 Direct numerical simulation and analysis of a spatially evolving supersonic turbulent boundary layer at $M = 2.25$. *Phys. Fluids* **16** (3), 530–545.

Ringuette, M. J., Martin, M. P., Smits, A. J. & Wu, M. 2006 Characterization of the turbulence structure in supersonic boundary layers using DNS data. *AIAA Paper* 2006-3539.

Ringuette, M. J., Wu, M. & Martin, M. P. 2008 Coherent structures in direct numerical simulation of turbulent boundary layers at Mach 3. *J. Fluid Mech.* **594**, 59–69.

Rubesin, M. W. 1990 Extra compressibility terms for Favre-averaged two-equation models of inhomogeneous turbulent flows. *Tech. Rep.* CR-177556. NASA.

Runstadler, P. S., Kline, S. J. & Reynolds, W. C. 1963 An experimental investigation of flow structure of the turbulent boundary layer. *Tech. Rep.* MD-8. Mechanical Engineering Department, Stanford University.

Smits, A. J. 1991 Turbulent boundary layer structure in supersonic flow. *Phil. Trans. R. Soc. Lond.* A **336** (1), 81–93.

Smits, A. J. & Dussauge, J. P. 2006 *Turbulent Shear Layers in Supersonic Flow*, 2nd edn. American Institute of Physics.

Spalart, P. R. 1988 Direct simulation of a turbulent boundary layer up to Re_θ equals 1410. *J. Fluid Mech.* **187**, 61–98.

Voisinet, R. L. P. & Lee, R. E. 1972 Measurements of a mach 4.9 zero-pressure-gradient turbulent boundary layer with heat transfer. Part 1. Data compilation. *Tech. Rep*. 0033757. Naval Ordnance Lab, White Oak, MD.

Walz, A. 1969 *Boundary Layers of Flow and Temperature*. MIT Press.

Xu, S. & Martin, M. P. 2004 Assessment of inflow boundary conditions for compressible turbulent boundary layers. *Phys. Fluids* **16** (7), 2623–2639.

Zhou, J., Adrian, R. J., Balachandar, S. & Kendall, T. M. 1999 Mechanisms for generating coherent packets of hairpin vortices in channel flow. *J. Fluid Mech.* **387**, 353–396.